Triple band diamond-shaped polarization insensitive plasmonic nano emitter for thermal camouflage and radiative cooling

Atıf Kerem Şanlı[1] · Timuçin Emre Tabaru[2,3,4] · Veli Tayfun Kılıç[1]

Abstract

This study proposes the design of a novel Metal-Insulator-Metal (MIM) nano-infrared emitter that uses a unique diamond-shaped grating to achieve selective infrared absorption. Diamond-shaped nano emitter (DNE) structure exhibits four narrow resonant peaks within key absorption windows such as short-wave infrared (SWIR) mid-wave infrared (MWIR), alongside with a wide absorption band in the Non-Transmissive Infrared Range (NTIR) for thermal camouflage applications compatible with radiative cooling. Moreover, the proposed DNE is polarization insensitive as it has an in-plane symmetric design. Using the 3D Finite-Difference Time-Domain (FDTD) simulations, we demonstrate the nanoantenna's superior performance characterized by its high absorption rates and tuned effective impedance matching. As of our knowledge, the findings suggest that this is the first time that a MIM structure achieved multiple narrow resonance peaks, located in SWIR and MWIR simultaneously, with a wide absorption range in NTIR. Represented DNE stands as a significant innovation in the field of stealth technology, providing a tunable, high-efficiency solution for managing and controlling thermal emissions across diverse applications.

Keywords Thermal camouflage · Mid-infrared · Thermal detection · Nanoantenna emitter · Metamaterial · Surface plasmon · Radiative cooling

✉ Timuçin Emre Tabaru
  etabaru@sivas.edu.tr

1   Department of Electrical and Electronics Engineering, Abdullah Gul University, Kayseri 38038, Türkiye

2   Departmanet of Electrical Electronic Engineering, Sivas University of Science and Technology, Mecnun Otyakmaz Street No:1, Sivas 58100, Türkiye

3   Institute of Materials Science Nanotechnology and National Nanotechnology Research Center (UNAM), Bilkent University, Ankara 06800, Türkiye

4   Clinical Engineering, Research and Application Center, Erciyes University, Kayseri 38019, Türkiye

🖄 Springer

1 Introduction

The increasing prevalence of the thermal imaging technologies in military applications has necessitated the development of effective thermal camouflaging techniques. According to Planck's law (Baranov et al. 2019; Zhu et al. 2020), every object that has a temperature above absolute zero, which is -273.15 °C, continues to radiate heat. This is crucial for such targets as aircraft, ground vehicles, and naval ships since some of their components can reach hundreds of degrees (Baranwal and Mahulikar 2016; Mahulikar et al. 2012; Thompson et al. 1998). Once the infrared trace created by components that belong to those are detected or tracked by thermal detection systems, thus they can be targeted by weaponry systems. It may seem straightforward to achieve thermal camouflage by blocking all emission wavelengths, such as using metallic foils or stainless steel. But according to the Stefan-Boltzmann Law ($P=\varepsilon\sigma T4$), the emission of an object is intrinsically tied to its surface emissivity (ε) (Buhara et al. 2021; Luo et al. 2019; Zhu et al. 2021), and Kirchoff's law further establishes that the absorptivity $\alpha(T, \lambda)$ of an object is equal to its emissivity $\varepsilon(T, \lambda)$ (Salihoglu et al. 2018; Tang et al. 2020). In contrast to these laws, since different atmospheric windows exist with different characteristics, using a full emission suppression method causes heat accumulation and instability issues (Buhara et al. 2021; Kim et al. 2019; Zhu et al. 2020). Thereby, a pathway for manipulating the absorption spectrum of nanoantennas to design efficient thermal emitters is needed. This can be achieved with an approach that emitted power must be selectively released into the atmosphere through specific wavelengths. The infrared region notably has two such regions: MWIR range of 3–5 μm and the long-wave infrared (LWIR) range of 8–12 μm. The NTIR is situated between these ranges, at 5–8 μm wavelengths, which is a region where high emission is needed to provide radiative cooling, different from the MWIR and LWIR. Additionally, SWIR cameras, which operate in the 1.4–3 μm range, are increasingly being used for target tracking (Cao et al. 2023; Lee et al. 2021; Sun et al. 2022). Therefore, for an object to ideally be infrared camouflaged, it should function as a good absorber in SWIR and NTIR, and as a reflector in MWIR and LWIR, which means the emission in MWIR and LWIR ranges must be suppressed. At the same time, absorption should be maximized in SWIR and NTIR atmospheric regions (Buhara et al. 2021; Huang et al. 2021; Ji et al. 2018; Kim et al. 2019). To achieve this, different types of metamaterials (Kang et al. 2024; Kim et al. 2017; Lee et al. 2019; Li et al. 2023). and multi-layer film structures (Salihoglu et al. 2018) have been presented, including MIM (Metal-Insulator-Metal) formations and phase-changing materials such as VO_2 and GST (Kang et al. 2021a, 2023; Kocer et al. 2021; Qu et al. 2018; Şanlı et al. 2022). In this study, we represent a simple, low-cost, easy-to-fabricate MIM nano infrared emitter device, which stands for metasurface with Diamond-shaped grating. The selection of materials for the nanoantenna structure, which includes silicon photonic technology, was made considering scalability, cost-effectiveness, and widespread availability, as well as compatibility with known CMOS fabrication methods. This approach provides ease of supply and lower production costs. Additionally, the relatively simple geometry of the nanoantenna structure suggests that its simplicity and standard lithography techniques can be used for fabrication. Although the claim of low cost and easy fabrication for nanoscale structures is generally debatable, the specific design choices made in this research, particularly the choice of CMOS-compatible materials and the simplicity of the geometry, support the feasibility of achieving cost-effectiveness. Detailed information on the effective fabrication of the pre-

sented MIM nanoantenna structure and the specific advantages and potential limitations of existing thermal camouflage technologies is provided in the supplementary document.

Emitters that have diamond-shaped gratings offer improved directionality of emission due to their pointed ends, which help focus emitted infrared light radiation along specific directions. Additionally, compared to circular shapes of the same footprint, diamond-shaped emitters boast a larger surface area, facilitating better heat dissipation crucial for maintaining efficiency. The sharp corners and edges of these emitters also support more plasmonic resonances, enhancing the local electromagnetic field and consequently increasing emission intensity.

Diamond-shaped Nano Emitter (DNE) consists of a unique design of Ag grating, Si_3N_4 dielectric, and Ag substrate. With this design, a promising approach is obtained to provide a suitable thermal camouflaging. To provide a more comprehensive understanding of the material selection process and its impact on the performance of the proposed structure, simulation studies were conducted with various metal and dielectric materials using them in the existing MIM structure. The results of these studies are given in the supplementary document. As can be understood from the results obtained, the most effective thermal camouflage was obtained with the recommended materials. Thanks to its amazing characteristics for radiative cooling, Ag is chosen as the grating material. This feature has an important role in achieving broadband absorption in the NTIR range. Si_3N_4 (Kischkat) is a dielectric used and referred to often in infrared camouflage applications (Lee et al. 2022; Li et al. 2023; Xiao et al. 2023). Characteristics of the presented DNE are simulated using a three-dimensional (3D) finite-difference time-domain (FDTD) tool. In the simulations, three narrow resonance peaks in SWIR at $\lambda_1 = 2.20$ μm, $\lambda_2 = 2.54$ μm, $\lambda_3 = 2.99$ μm, and one in the MWIR window which is at $\lambda_4 = 3.99$ μm, are observed. Also, a broadband absorption is achieved in the NTIR window at $\lambda_5 = 7.4$ μm. These narrow resonance peaks in SWIR and MWIR provide more than 90% absorption, also more than 97% absorption is observed in the NTIR window. As of our knowledge, this is the first study that employs this much narrow resonance peaks, located in SWIR and MWIR ranges simultaneously, with a wide absorption band located in the NTIR window.

2 Theory and design

Figure 1(a) shows the single unit cell of DNE and Fig. 1(b) is the array sheet of DNE structure. This structure is based on an Ag substrate with a height of *"H₁"* and the dielectric layer which is Si_3N_4 has a height of *"H₂"*. Lastly, the grating part of the structure with diamond-shaped Ag comes, with a thickness of *"t"* and a side length of *"N"*. Structure is periodic in the x and y axis with the value of *"P"*. To achieve optimal values, single parameter sweep analysis for grating thickness, grating side length, and structure periodicity are performed first, as shown in Fig. 2(a-c) as a function of absorption. After the single parameter analysis, dual parameter sweeps are performed for related wavelength resonance peaks which are λ_1, λ_2, λ_3, λ_4, and λ_5 respectively. Figure 3(a-e), represents the contour plots of grating thickness and periodicity of the structure. With that, compatibility of the parameters with each other and with atmospheric absorption wavelengths was examined. Thus, parameters are determined as, H_1 is 100 nm, H_2 is 350 nm, *t* is 20 nm, *N* is 900 nm and *P* is 2090 nm. Boundary conditions are chosen as periodic in the x and y-axis, and PML (Perfect Match Layer) in the
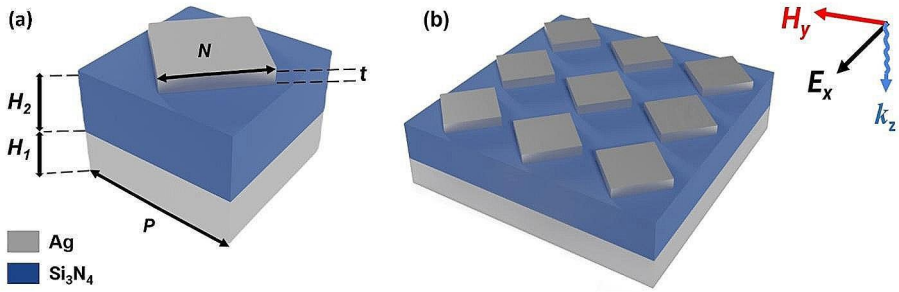
Fig. 1 Schematic design of the presented nanoantenna. (**a**) Perspective view of the presented nanoantenna unit cell, (**b**) 3D view of the nanoantenna array sheet
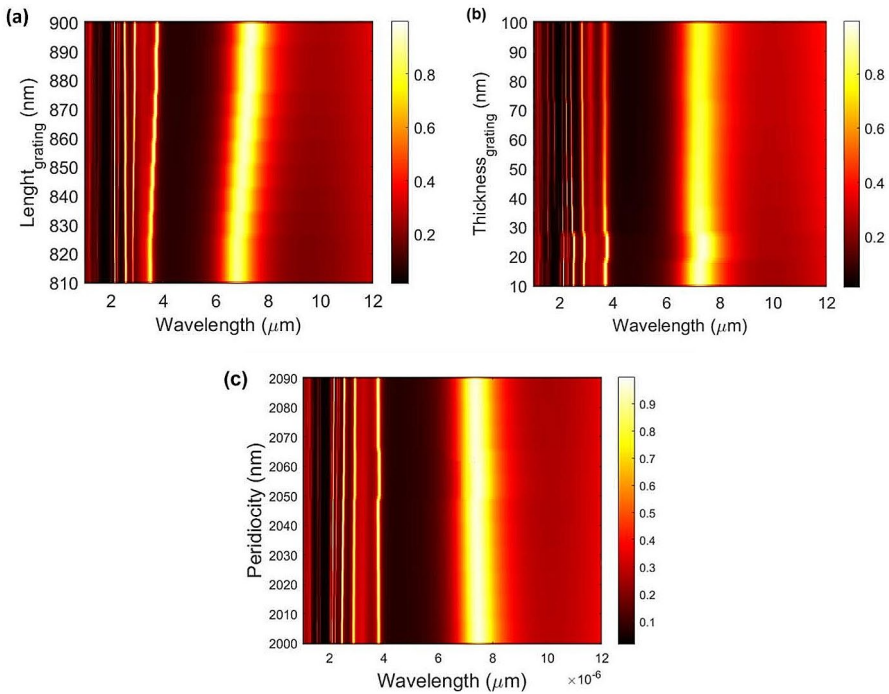
Fig. 2 (**a-c**) Contour plots of the single parameter sweep analysis of designed DNE calculated for various grating thickness, grating side length N, and periodicity P against wavelength

z-axis. TM polarized plane wave light source in the wavelengths between 1 and 12 μm is placed above the structure. To obtain reflection and transmission data, reflectance and transmission monitors are placed above the light source and below the structure, respectively.

As it can be seen from Fig. 2(a), value of side length of grating *"N"* directly affects the position of wide band NTIR resonance peak (λ_5), causing a shift to higher wavelengths. Also, similar shift observed for resonance peak in MWIR (λ_4). Meanwhile, thickness of
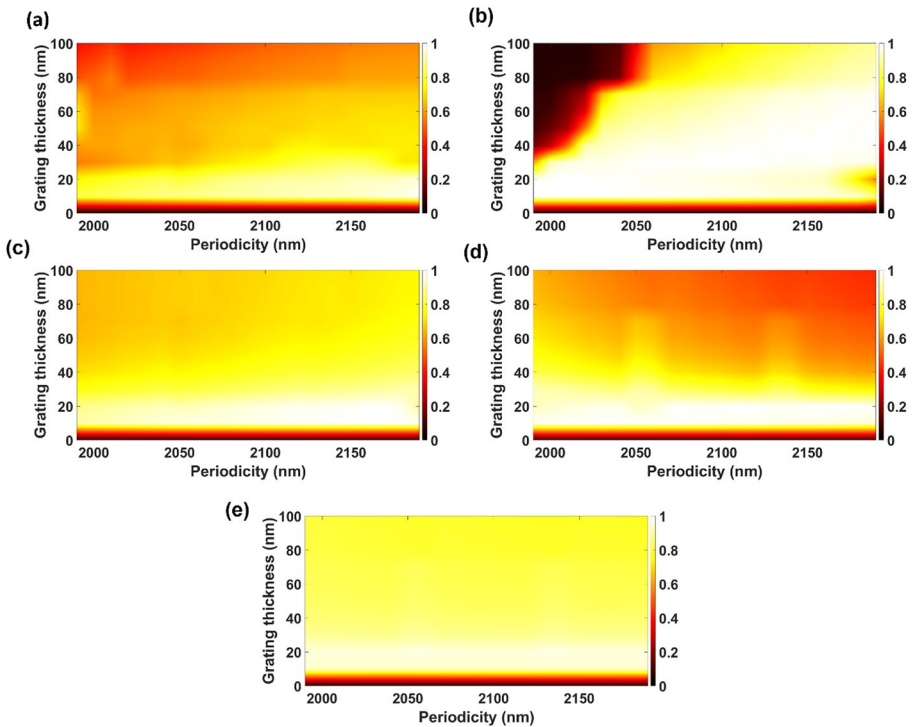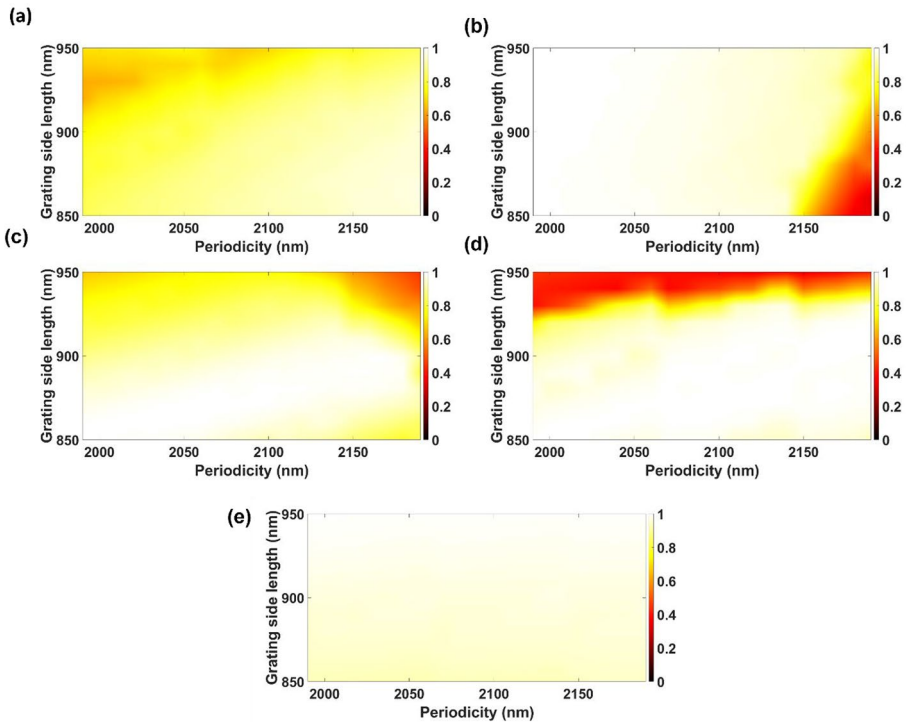
Fig. 3 (**a-e**) Contour plots of the dual parameter sweep analysis of designed DNE calculated for various grating thickness t against periodicity P for given wavelengths λ_1, λ_2, λ_3, λ_4, and λ_5 respectively. Color bars represent the absorption

grating and periodicity does not directly affect the position or the amplitude of the resonance peaks as a function of absorption, individually.

After observing the direct effect of grating side length, thickness and periodicity of DNE, we decided to further investigate the dual parameter affects as function of absorption, staring from thickness of grating and the periodicity of DNE simultaneously. Figure 3(a-e) illustrates contour plots of the grating thickness and the values of periodicity of DNE varying with each other, as a function of amplitude of absorption. For NTIR resonance peak (λ_5), DNE shows approximately %90 absorption amplitude for almost every case where there is a grating exist. On the other hand, for other resonance peaks, DNE shows different amplitudes for different thickness and periodicity values.

Figure 4 (a-e) illustrates contour plots of the grating side length and the periodicity of values of periodicity of DNE varying with each other, as a function of amplitude of absorption. Similarly, for NTIR resonance peak (λ_5), DNE shows approximately %95 absorption amplitude for almost every case. For the other resonances, DNE shows near-unity absorption for a wide range of side length and periodicity values. This is also another privilege that presents a flexible design. On the other hand, despite of the high absorption amplitudes, in some cases, it is observed that the resonance peaks may shift out of the desired infrared windows. Thus, in order to achieve the highest absorption amplitudes in the desired infrared

Fig. 4 (**a–e**) Contour plots of the dual parameter sweep analysis of designed DNE calculated for various grating side length N against periodicity P for given wavelengths λ_1, λ_2, λ_3, λ_4, and λ_5 respectively. Color bars represent the absorption

windows, the parameters are optimized and selected as t is 20 nm, N is 900 nm and P is 2090 nm.

3 Results and discussions

Figure 5(a) shows the different infrared regions in the investigated wavelength range. After all the optimizations mentioned in the previous section, represented absorption behavior of DNE has been achieved as shown in Fig. 5(b). There are four narrow peaks at $\lambda_1 = 2.20$ μm, $\lambda_2 = 2.54$ μm, $\lambda_3 = 2.99$ μm, and at $\lambda_4 = 3.99$ μm with more than %90 of absorption, is observed. Also, a broadband resonance peak with more than %97 absorption is achieved in the NTIR window at $\lambda_5 = 7.4$ μm. These results not only point out multiple atmospheric absorption cases of DNE but also show a good cooling character.

Although MWIR is typically the area where low emissivity is needed, the placement of λ_4 within the atmospheric absorption window (Buhara et al. 2021) enhances the material's ability to blend with the background thermal signature, contributing to effective camouflage (Yao et al. 2023). The emissivity value obtained in the LWIR region is a value that can be seen in the studies presented in the literature (Buhara et al. 2021; Qian et al. 2023; Zhang et al. 2021), and in the article presented, the average emissivity value is seen to remain 0.33
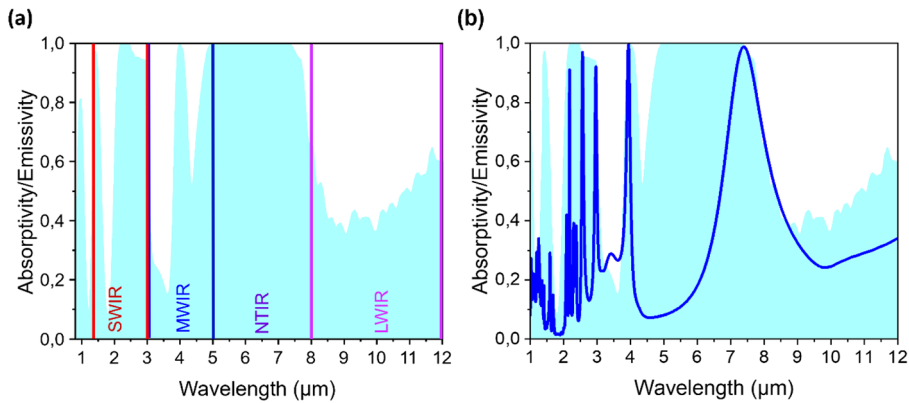
Fig. 5 (**a**) IR atmospheric regions, (**b**) absorption behavior of DNE related with the IR atmospheric regions at given wavelengths λ_1, λ_2, λ_3, λ_4, and λ_5 respectively

and below even at 1000 K temperature as seen in Fig. 6 (a). Therefore, the stated value is considered to be negligible. The strategic design of materials with tailored emissivity profiles, such as the proposed DNE, can deceive IR signatures and regulate thermal appearance for enhanced camouflage performance.

To examine the physical mechanisms of the nanoantenna, electrical field and magnetic field distribution profiles for represented resonance wavelengths, involving a plane wave illumination, have been extracted as shown in Figs. 7 and 8, from the top and front view. In the case of every resonance wavelength, one can observe that there is a significant electrical field enhancement, located between plasmonic (Ag) grating and dielectric interface, mostly focused on the corners of grating. This represents the existence of surface plasmon polaritons (SPPs) (Aslan et al. 2017; Lee et al. 2021; Zhang et al. 2012).

Also, in some cases, it is possible to observe a portion of light trapped inside a dielectric layer, such as in Fig. 7(b). By looking at it, one can see that Fabry-Perot mode also occurs at λ_2, which further provides a bulk absorption in the Si_3N_4 dielectric layer. Furthermore, inspection of the intensity values, as represented by the color bar plots, indicates varying field intensities across the grating and the whole structure. These field distribution analysis not only highlight the magnitude of the fields at specific regions but also provide insights into the different optical phenomena, occurring at the grating and inside of the dielectric layer.

Next, the effective impedance of the nanoantenna is calculated by using S-parameters (scattering parameters), which are obtained from port analysis simulations, done with the 3D FDTD tool. Absorption can be expressed as $A = 1 - T - R$, thus, using the S - parameters reflection can be represented as $R = |S_{11}|^2$ and transmission can be represented as $T = |S_{21}|^2$. Since we use a metal substrate, nearly zero transmission is observed, so S_{21} is considered as zero. As a result, the absorption can be determined as $A = 1 - R$, which also can be written as $A = 1 - |S_{11}|^2$, so the Eq. (1) (Xiao et al. 2023) can be simplified to Eq. (2). After clarifying these expressions, it is possible achieve the effective impedance using the Eq. (2):
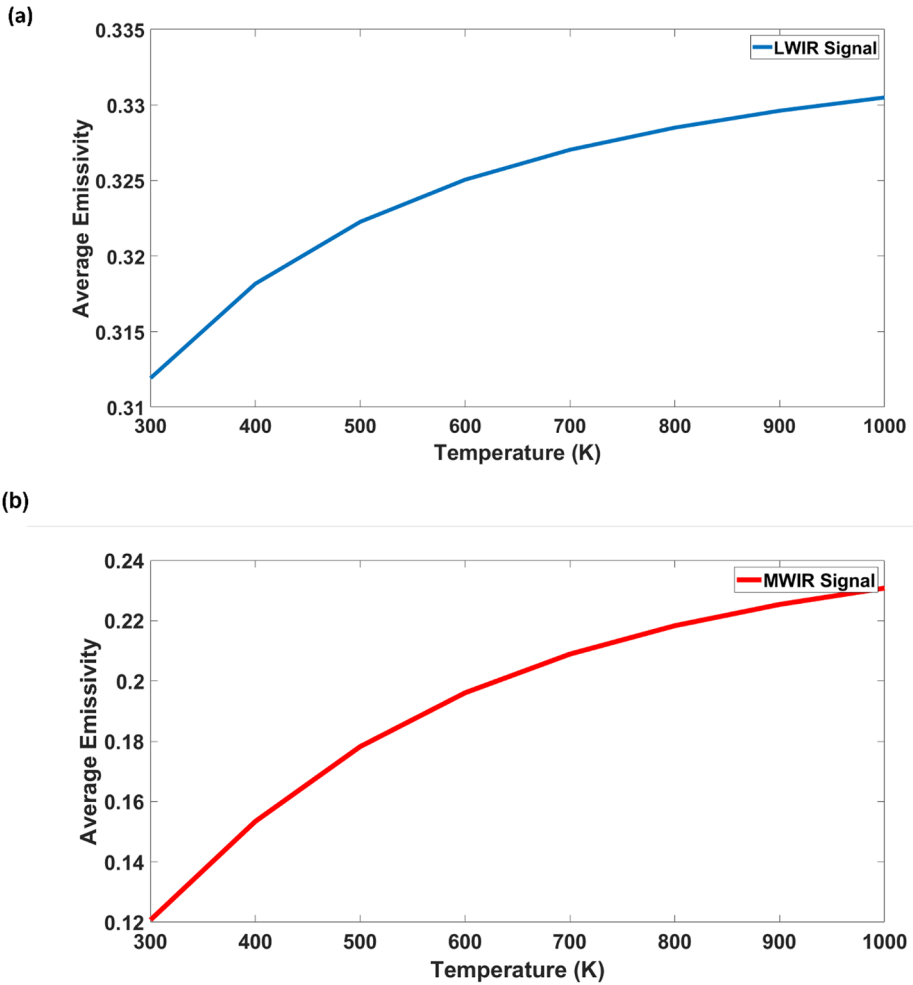
(a)

(b)

Fig. 6 (**a**), (**b**). MWIR and LWIR signature analysis of DNE by calculating its average thermal emission

$$Z_{eff} = \sqrt{\frac{(1 + S_{11})^2 - S_{21}^2}{(1 - S_{11})^2 - S_{21}^2}} \qquad (1)$$

$$Z_{eff} = \sqrt{\frac{(1 + S_{11})^2}{(1 - S_{11})^2}} \qquad (2)$$

Figure 9(a) illustrates the effective impedance of the nanoantenna for the inspected wavelength region of 1–12 μm. The effective impedances of observed resonance wavelengths are almost matching completely with the effective impedance of the surrounding air. This means that at these wavelengths there is almost no reflection, and since the nanoantenna
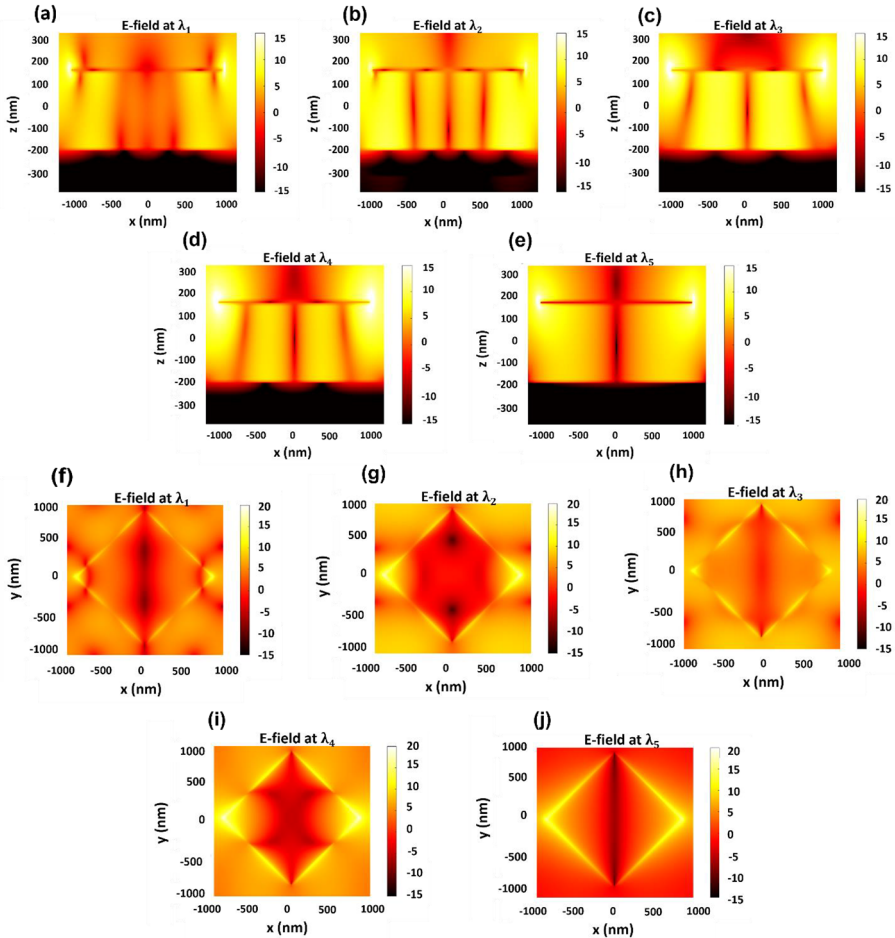
Fig. 7 (**a**) – (**e**) E-field distribution plot of nanoantenna from front view, (**f**) – (**j**) E-field distribution plot of nanoantenna from top view for $\lambda_1, \lambda_2, \lambda_3, \lambda_4, \lambda_5$, respectively
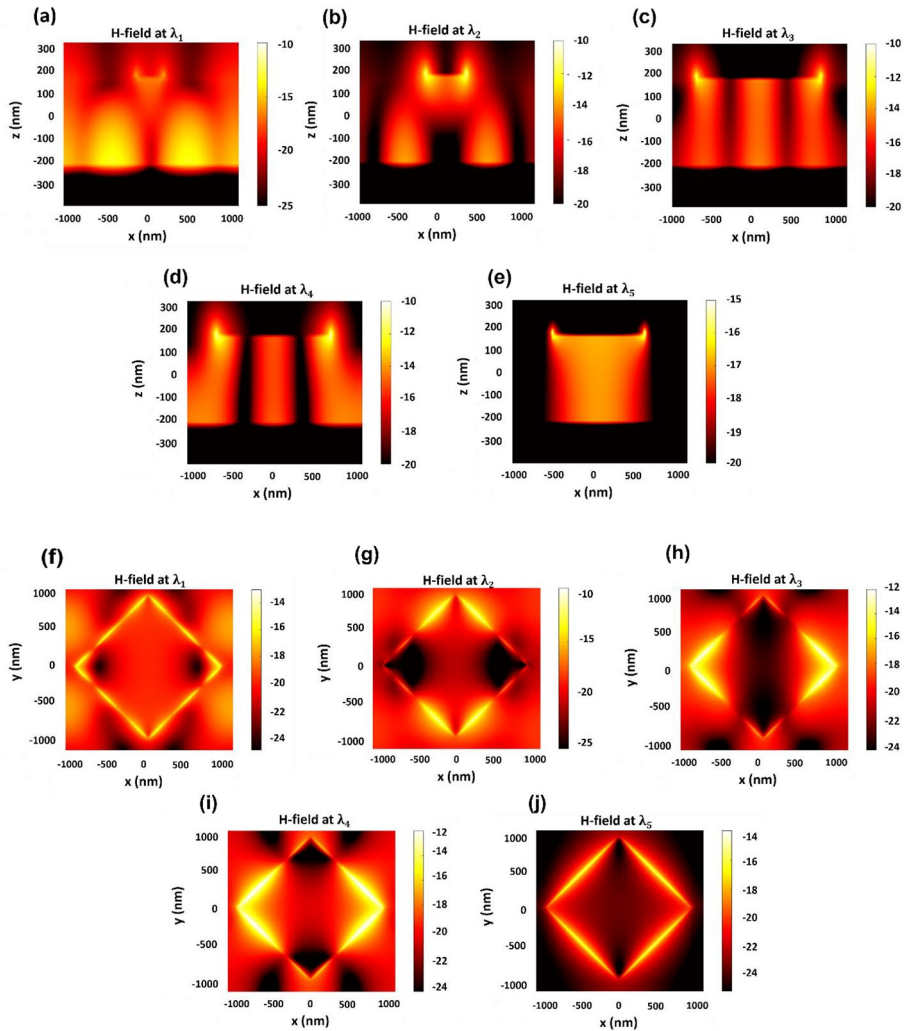
also shows no transmission, it is possible to see a significant absorption at the represented wavelengths.

$$\epsilon_{eff}(T, \lambda) = \sum_{J=1}^{3} \epsilon_j(T, \lambda) \qquad (3)$$

$$\epsilon_1(T, \lambda) = 1 - R(T, \lambda) - T(T, \lambda) \qquad (4)$$

$$\epsilon_2(T, \lambda) = (1 - \epsilon_{blackbody}) T_{back}(T, \lambda) \epsilon_1(T, \lambda) \qquad (5)$$

$$\epsilon_3(T, \lambda) = T_{back}(T, \lambda) \epsilon_{blackbody} \qquad (6)$$

Fig. 8 (**a**) – (**e**) H-field distribution plot of nanoantenna from front view, (**f**) – (**j**) H-field distribution plot of nanoantenna from top view for $\lambda_1, \lambda_2, \lambda_3, \lambda_4, \lambda_5$, respectively

$$BBE\left(T, \lambda\right) = \frac{2\pi hc^2}{\lambda^5(e^{\frac{hc}{\lambda kT}} - 1)} \qquad (7)$$

$$TE\left(T, \lambda\right) = \epsilon_{eff}\left(T, \lambda\right) \times BBE\left(T, \lambda\right) \qquad (8)$$

Figure 9(b) shows the theoretical calculation of the thermal emission of DNE and the black-body radiation at 300 K (For high and ultra-high temperatures, see Fig. S1 in the supplementary document). The thermal emission of DNE and blackbody emitter (BBE) is calculated using Eqs. (3–8), where *"T"* is the temperature, *"λ"* is wavelength, *"ϵ"* is emission (Buhara
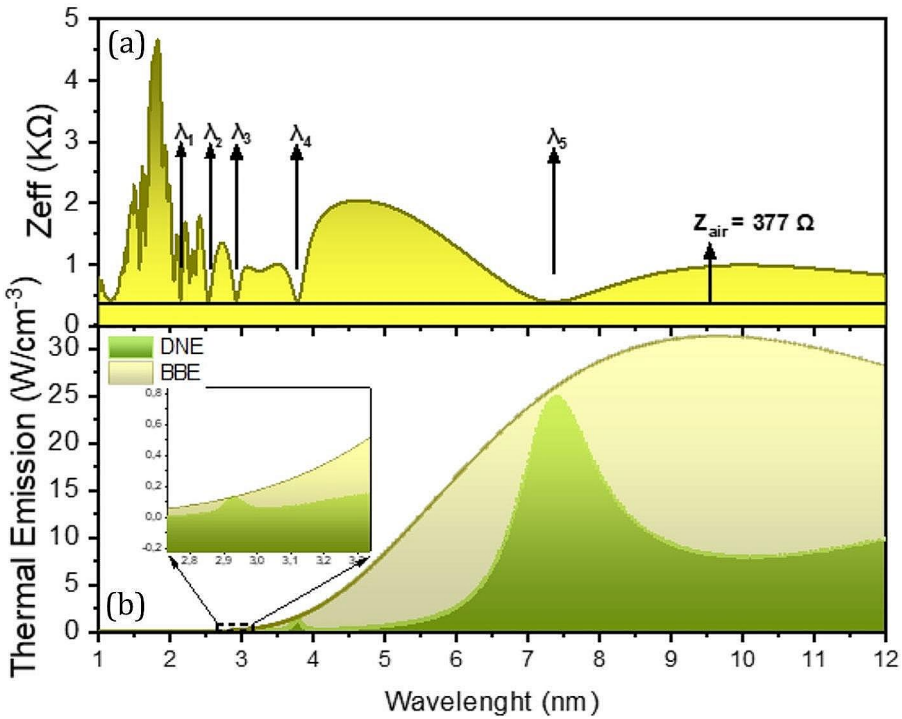
Fig. 9 (**a**) Effective Impedance values calculated against wavelength. The effective impedance of air (377Ω) and the peak wavelengths of the presented DNE structure are indicated. (**b**) Comparison of thermal emission of DNE and blackbody radiation at room temperature

et al. 2021). With this approach, thermal emission of an application, which contains the BBE and DNE can be calculated. Three emissions should be calculated to get the total thermal emission of potential application. The first one is the emission of DNE, calculated in Eq. (3). Second is the emission that transmits into the DNE, reflects from the BBE and transmits backward to the surface of, calculated in Eq. (4). Lastly, the third emission is the blackbody emission which is created in the hot object and transmits through the DNE, calculated in Eq. (5). Sum of these three emissions (Eqs. 3–5), is the effective emission (Eq. 2). After calculating the blackbody radiation using Eq. (6), and multiplying it with Eq. (2), it is possible to calculate the total thermal emission of the application, which is shown in Eq. (7). As result of these calculations, one can observe from Fig. 9(b), DNE structure has a significant signature reduction in MWIR (3–5 μm) and LWIR (8–12 μm) where the calculated thermal emission remains under the BBE's thermal emission, and also has a strong cooling characteristic, which can be observed from the amount of thermal emission in NTIR (5–8 μm).

Lastly, thermal signature reduction abilities of DNE for various temperature levels have been investigated by calculating average thermal emission between a depicted wavelength range using Eq. (8) (Wang et al. 2021)

$$\epsilon[\lambda_1, \lambda_2]_{avg} = \int_{\lambda_1}^{\lambda_2} \epsilon(\lambda) \, I_{BB}(\lambda, T) \, d\lambda / \int_{\lambda_1}^{\lambda_2} I_{BB}(\lambda, T) \, d\lambda$$

$I_{BB}(\lambda, T) = 2hc^2/\lambda^5 \cdot [exp(hc/\lambda k_B T) - 1]^{-1}$ is the radiated energy of a blackbody at a wavelength of λ and temperature of T according to Planck's law. Average thermal emission of DNE in MWIR and LWIR regions is shown in Fig. 6. Temperature values start from 300 K and up to 1000 K. Despite the increasing temperature, DNE shows suitable signature reduction for both MWIR and LWIR regions.

Here in, we list some recently reported results in the field of multi-band camouflage in Table 1. While Kim et al. 2022; Zhu et al. 2021; Pan et al. 2020 and Jiang et al. 2023 provide relatively effective signature reduction in MWIR and LWIR, the majority of the reported works do not achieve the compatibility of narrow band SWIR camouflage characteristics and other camouflage bands. The simple DNE structure in this work, however, provides SWIR camouflage by multiple narrow band absorption peaks, and also compatible with other camouflage requirements, and provides excellent performance in each band.

4 Conclusions

In conclusion, the research presented in this letter introduces a novel MIM nanoantenna structure with a distinctive Diamond-shaped Ag grating, optimized for thermal camouflaging applications. By exploiting the unique properties of Ag and Si_3N_4 in the design, the structure achieves significant absorption rates of over 90% in SWIR and MWIR with narrow resonance peaks and above 97% in the NTIR window with a wide band resonance peak. The simulations using the 3D FDTD tool validate the efficacy of this design, showing negligible transmission and near-zero effective impedance at resonance peaks, indicating strong absorption. Field distribution profiles show the significant enhancement of fields and physical mechanisms contributing to these results, such as SPPs and Fabry-Perot modes are also evident. These findings suggest that the presented DNE can effectively manage thermal signatures by selective emission, opening new opportunities for thermal camouflage that could significantly impact military and surveillance strategies and other infrared-based technologies. This innovative technology offers several advantages over existing solutions, including enhanced spectral control, dynamic adaptability, reduced thickness and weight, and integration with existing materials. The nano-scale design allows for precise control over spectral characteristics, improving camouflage effectiveness, while also enabling dynamic changes in thermal emission properties for real-time adaptability. Furthermore, the

Table 1 Comparison of the recently reported results for multi-band camouflage with this work, MFS: Multi-layer Film Structures

Ref.	Materials	Structure	SWIR Narrow Band Camouflage			Thermal Camouflage		Thermal Management
			$\alpha_{2.20\,\mu m}$	$\alpha_{2.54\,\mu m}$	$\alpha_{2.99\,\mu m}$	ε_{MWIR}	ε_{LWIR}	$\varepsilon_{5\sim8}$
Our Work	Ag/Si_3N_4	Metamaterial	0.91	0.96	0.92	0.17	0.32	0.44
(Kim et al. 2022)	Al/Ge/Ag	Metamaterial	×	×	×	0.06	0.02	×
(Pan et al. 2020)	GST/Si/Au	Metamaterial	×	×	×	0.25	0.33	0.77
(Zhu et al. 2021)	Ge/ZnS	9-Layer MFS	×	×	×	×	0.02	0.575
(Yan et al. 2023)	Ge/SiO_2/Pt/ZnS	7-Layer MFS	×	×	×	0.21	0.16	0.54

development of thinner, lighter materials is crucial for applications in wearable technology and UAVs. However, potential limitations include fabrication complexity, durability concerns due to susceptibility to damage, scalability challenges in large-area production, and integration difficulties with existing materials, highlighting the need for further research and development to address these issues.

Data availability No datasets were generated or analysed during the current study.

Declarations

Conflict of interest The authors declare that they have no competing interests.

References

Aslan, E., Aslan, E., Turkmen, M., Saracoglu, O.G.: Experimental and numerical characterization of a mid-infrared plasmonic perfect absorber for dual-band enhanced vibrational spectroscopy. Opt. Mater. (Amst). **73**, 213–222 (2017). https://doi.org/10.1016/J.OPTMAT.2017.08.023

Baranov, D.G., Xiao, Y., Nechepurenko, I.A., Krasnok, A., Alù, A., Kats, M.A.: Nanophotonic engineering of far-field thermal emitters. Nat. Mater. 2019 189. **18**, 920–930 (2019). https://doi.org/10.1038/s41563-019-0363-y

Baranwal, N., Mahulikar, S.P.: Infrared signature of aircraft engine with choked converging nozzle. J. Thermophys. Heat. Transf. **30**, 854–862 (2016). https://doi.org/10.2514/1.T4641/ASSET/IMAGES/LARGE/FIGURE8.JPEG

Buhara, E., Ghobadi, A., Ozbay, E.: Multi-spectral infrared camouflage through excitation of plasmon-phonon polaritons in a visible-transparent hBN-ITO nanoantenna emitter. Opt. Lett. Vol. **46**, 4996–4999 (2021). https://doi.org/10.1364/OL.437933

Buhara, E., Osgouei, A.K., Khalichi, B., Kocer, H., Ghobadi, A., Ozbay, E.: Thermally Tunable from Narrowband to Broadband Metamaterial-Based Nanoantenna Emitter. 2021 IEEE Photonics Conf. IPC 2021 - Proc. (2021). https://doi.org/10.1109/IPC48725.2021.9592928

Cao, P., Wang, T., Peng, H., Zhuang, Q., Zheng, W.: Growth and Dark Current Analysis of GaSb- and InP-Based Metamorphic In0.8Ga0.2As Photodetectors. Mater. Vol. 16, Page 4538. 16, 4538 (2023). (2023). https://doi.org/10.3390/MA16134538

Huang, Y., Ma, B., Pattanayak, A., Kaur, S., Qiu, M., Li, Q.: Laser Photon Rev. 15, 2000391 (2021). https://doi.org/10.1002/LPOR.202000391 Infrared Camouflage Utilizing Ultrathin Flexible Large-Scale High-Temperature-Tolerant Lambertian Surfaces

Jiang, X., Yuan, H., He, X., Du, T., Ma, H., Li, X., Luo, M., Zhang, Z., Zhu, G., Kang, Q., Guo, K., Guo, Z.: A tunable infrared emitter based on phase-changing material GST for visible-infrared compatible camouflage with thermal management. Phys. Chem. Chem. Phys. 25, 27668?27676 (2023). https://doi.org/10.1039/D3CP02983B

Ji, H., Liu, D., Cheng, H., Zhang, C., Yang, L.: Vanadium dioxide nanopowders with tunable emissivity for adaptive infrared camouflage in both thermal atmospheric windows. Sol Energy Mater. Sol Cells. 175, 96–101 (2018). https://doi.org/10.1016/J.SOLMAT.2017.10.013

Kang, Q., Guo, K., Guo, Z.: A tunable infrared emitter based on phase-changing material GST for visible-infrared compatible camouflage with thermal management. Phys. Chem. Chem. Phys. 25, 27668–27676 (2023). https://doi.org/10.1039/D3CP02983B

Kang, Q., Guo, K., Guo, Z.: Polarization manipulations of Mid-infrared Thermal Emission enabled by Plasmonic Metasurfaces. IEEE Photonics Technol. Lett. 36, 199–202 (2024). https://doi.org/10.1109/LPT.2023.3345951

Kang, Q., Li, D., Guo, K., Gao, J., Guo, Z.: Tunable Thermal Camouflage Based on GST Plasmonic Metamaterial. Nanomater. Vol. 11, Page 260. 11, 260 (2021a)(a). (2021). https://doi.org/10.3390/NANO11020260

Kim, H.Y., Yoo, T.H., Hwang, Y., Lee, G.H., Kim, B., Jang, J., Yu, H.T., Kim, M.C., Cho, J.Y., Lee, C.J., Kim, H.C., Park, S., Lee, W.W.: Indoxyl sulfate (IS)-mediated immune dysfunction provokes endothelial damage in patients with end-stage renal disease (ESRD). Sci. Rep. 2017 71. 71–16 (2017). https://doi.org/10.1038/s41598-017-03130-z

Kim, J., Park, C., Hahn, J.W., Kim, J., Park, C., Hahn, J.W.: Metal–Semiconductor–Metal Metasurface for Multiband Infrared Stealth Technology using camouflage Color Pattern in visible range. Adv. Opt. Mater. 10, 2101930 (2022). https://doi.org/10.1002/ADOM.202101930

Kim, T., Bae, J.-Y., Lee, N., Cho, H.H., Semiconductor, T.K., Center, R., Bae, J.-Y., Lee, N., Cho, H.: Hierarchical metamaterials for Multispectral Camouflage of Infrared and microwaves. Adv. Funct. Mater. 29, 1807319 (2019). https://doi.org/10.1002/ADFM.201807319

Kocer, H., Cakir, M.C., Durna, Y., Soydan, M.C., Odabasi, O., Isik, H., Aydin, K., Ozbay, E.: Exceptional adaptable MWIR thermal emission for ordinary objects covered with thin VO2 film. J. Quant. Spectrosc. Radiat. Transf. 262, 107500 (2021). https://doi.org/10.1016/J.JQSRT.2020.107500

Lee, N., Kim, T., Lim, J.S., Chang, I., Cho, H.H.: Metamaterial-selective emitter for maximizing Infrared Camouflage performance with Energy Dissipation. ACS Appl. Mater. Interfaces. 11, 21250–21257 (2019). https://doi.org/10.1021/ACSAMI.9B04478/SUPPL_FILE/AM9B04478_SI_001.PDF

Lee, N., Lim, J.-S., Chang, I., Bae, M., Nam, H., Cho, J., Lee, H.H., Lim, N., Chang, J.-S., Bae, I., Nam, H.M., Cho, J.: Flexible assembled metamaterials for Infrared and Microwave Camouflage. Adv. Opt. Mater. 10, 2200448 (2022). https://doi.org/10.1002/ADOM.202200448

Lee, N., Lim, J.S., Chang, I., Lee, D., Cho, H.H.: Transparent metamaterials for Multispectral Camouflage with Thermal Management. Int. J. Heat. Mass. Transf. 173, 121173 (2021). https://doi.org/10.1016/J.IJHEATMASSTRANSFER.2021.121173

Li, J., Liu, S., Wu, S., Zhong, A.Z.: Metamaterials-based broadband absorption in long-wave infrared frequency enabled by multilayered ENZ films on metal-coated patterned silicon. Opt. Express, 31, 8453–8464 (2023). https://doi.org/10.1364/OE.482653

Luo, H., Li, Q., Du, K., Xu, Z., Zhu, H., Liu, D., Cai, L., Ghosh, P., Qiu, M.: An ultra-thin colored textile with simultaneous solar and passive heating abilities. Nano Energy. 65, 103998 (2019). https://doi.org/10.1016/J.NANOEN.2019.103998

Mahulikar, S.P., Rao, G.A., Kolhe, P.S.: Infrared signatures of low-flying aircraft and their rear fuselage skin's Emissivity optimization. J. Aircr. 43, 226–232 (2012). https://doi.org/10.2514/1.15365

Pan, M., Huang, Y., Li, Q., Luo, H., Zhu, H., Kaur, S., Qiu, M.: Multi-band middle-infrared-compatible camouflage with thermal management via simple photonic structures. Nano Energy. 69, 104449 (2020). https://doi.org/10.1016/J.NANOEN.2020.104449

Qian, M., Shi, Q., Qin, L., Huang, J., Guo, C., Liu, Y., Yu, K.: Fabrication of selective thermal emitter with multilayer films for mid-/low-temperature infrared stealth with radiative cooling. Photonics. 10, 645 (2023). https://doi.org/10.3390/photonics10060645

Qu, Y., Li, Q., Cai, L., Pan, M., Ghosh, P., Du, K., Qiu, M.: Thermal camouflage based on the phase-changing material GST. Light Sci. Appl. 2018 71. 7, 1–10 (2018). https://doi.org/10.1038/s41377-018-0038-5

Salihoglu, O., Uzlu, H.B., Yakar, O., Aas, S., Balci, O., Kakenov, N., Balci, S., Olcum, S., Süzer, S., Koca-bas, C.: Graphene-based adaptive thermal camouflage. Nano Lett. **18**, 4541–4548 (2018). https://doi.org/10.1021/ACS.NANOLETT.8B01746/SUPPL_FILE/NL8B01746_SI_004.AVI

Şanlı, A.K., Tabaru, T.E., Kılıç, V.T.: Design of Wavelength selectively Metamaterial Antenna for Thermal Camouflage. Eur. J. Res. Dev. **2**, 90–97 (2022). https://doi.org/10.56038/EJRND.V2I4.181

Sun, K., Vassos, E., Yan, X., Wheeler, C., Churm, J., Wiecha, P.R., Gregory, S.A., Feresidis, A., de Groot, C.H., Muskens, O.L.: Wafer-scale 200 mm metal Oxide Infrared Metasurface with tailored Differential Emissivity response in the Atmospheric Windows. Adv. Opt. Mater. **10**, 2200452 (2022). https://doi.org/10.1002/ADOM.202200452

Tang, K., Wang, X., Dong, K., Li, Y., Li, J., Sun, B., Zhang, X., Dames, C., Qiu, C., Yao, J., Wu, J., Tang, K., Wang, X., Dong, K., Li, J., Yao, J., Wu, J., Zhang, X., Li, Y., Qiu, C., Sun, B., Dames, C.: A Thermal Radiation Modulation platform by Emissivity Engineering with Graded metal–insulator transition. Adv. Mater. **32**, 1907071 (2020). https://doi.org/10.1002/ADMA.201907071

Thompson, J., Vaitekunas, D., Birk, A.M.: IR signature suppression of modern naval ships. In: ASNE 21st century combatant technology symposium. p. Vol. 1, pp. 27–30 (1998)

Xiao, G., Lai, Z., Yang, H., Wang, B., Li, H.: Tunable environment-enhanced mid-infrared Absorber based on voltage modulation. IEEE Photonics J. **15** (2023). https://doi.org/10.1109/JPHOT.2023.3300535

Yan, P., Wu, J., Zhang, Z., Yang, J.: Implementing of infrared camouflage with thermal management based on inverse design and hierarchical metamaterial. Nanophotonics. **12**, 1891–1902 (2023). https://doi.org/10.1515/NANOPH-2023-0067

Yao, L., Pan, L., Zhou, S., Liu, H., Mei, H., Li, Y., Dassios, K.G., Colombo, P., Cheng, L., Zhang, L.: Wide-temperature-range multispectral camouflage enabled by orientation-gradient co-optimized microwave blackbody metastructure coupled with conformal MXene coating. Mater. Horizons. **10**, 3404–3415 (2023). https://doi.org/10.1039/D3MH00611E

Zhang, J., Zhang, L., Xu, W.: Surface plasmon polaritons: Physics and applications. J. Phys. D Appl. Phys. **45**, 113001 (2012). https://doi.org/10.1088/0022-3727/45/11/113001

Zhang, L., et al.: A thermally robust and optically transparent infrared selective emitter for compatible cam-ouflage. J. Mater. Chem. C. **9**, 15018–15025 (2021). https://doi.org/10.1039/D1TC02953C

Zhu, H., Li, Q., Tao, C. et al.: Multispectral camouflage for infrared, visible, lasers and microwave with radia-tive cooling. Nat. Commun. **12**, 1805 (2021). https://doi.org/10.1038/s41467-021-22051-0

Zhu, H., Li, Q., Zheng, C., Hong, Y., Xu, Z., Wang, H., Shen, W., Kaur, S., Ghosh, P., Qiu, M.: High-temperature infrared camouflage with efficient thermal management. Light Sci. Appl. 2020 91. 91–8 (2020). https://doi.org/10.1038/s41377-020-0300-5

Wang, L., et al.: Combined multi-band infrared camouflage and thermal management via a simple multilayer structure design. Optics Lett. **46**, 5224–5227 (2021). https://doi.org/10.1364/OL.441605